

Modification of Two-Dimensional Tin-Based Perovskites by Pentanoic Acid for Improved Performance of Field-Effect Transistors

Shuanglong Wang, Konstantinos Bidinakis, Constantin Haese, Franziska H. Hasenburg, Okan Yildiz, Zhitian Ling, Sabine Frisch, Milan Kivala, Robert Graf, Paul W. M. Blom, Stefan A. L. Weber, Wojciech Pisula,* and Tomasz Marszalek*

Understanding and controlling the nucleation and crystallization in solution-processed perovskite thin films are critical to achieving high in-plane charge carrier transport in field-effect transistors (FETs). This work demonstrates a simple and effective additive engineering strategy using pentanoic acid (PA). Here, PA is introduced to both modulate the crystallization process and improve the charge carrier transport in 2D 2-thiopheneethylammonium tin iodide ((TEA)₂SnI₄) perovskite FETs. It is revealed that the carboxylic group of PA is strongly coordinated to the spacer cation TEA⁺ and [SnI₆]⁴⁻ framework in the perovskite precursor solution, inducing heterogeneous nucleation and lowering undesired oxidation of Sn²⁺ during the film formation. These factors contribute to a reduced defect density and improved film morphology, including lower surface roughness and larger grain size, resulting in overall enhanced transistor performance. The reduced defect density and decreased ion migration lead to a higher p-channel charge carrier mobility of 0.7 cm² V⁻¹ s⁻¹, which is more than a threefold increase compared with the control device. Temperature-dependent charge transport studies demonstrate a mobility of 2.3 cm² V⁻¹ s⁻¹ at 100 K due to the diminished ion mobility at low temperatures. This result illustrates that the additive strategy bears great potential to realize high-performance Sn-based perovskite FETs.

facile processability.^[1,2] However, the application of perovskites in field-effect transistors (FETs) has received less attention and has remained challenging because of ion migration under operational conditions at room temperature due to the low formation energy of mobile ions or ionic defects in these ionic materials.^[3,4] Mobile ions in perovskite FETs screen the applied gate field and reduce the gate modulation of the current yielding low field-effect mobility and large hysteresis.^[5] In contrast, 2D Sn-based perovskites reveal favorable properties due to the insulating property of bulky organic ligands. The advantages of dielectric confinement in 2D layered structures are expected to significantly suppress ion movement in the device.^[6] More importantly, the device performance can be tuned by tailoring the chemical structure of the spacer cations.^[7]

2D Sn-based perovskites are promising semiconductors for high-performance FETs.^[8,9] The Sn-based perovskites typically show high charge carrier mobility due to the smaller in-plane effective mass

and longer carrier lifetime compared with their Pb analogs.^[10] Nevertheless, there are several drawbacks to 2D Sn-based perovskite FETs. First, easy oxidation of Sn²⁺ to its tetravalent state Sn⁴⁺, especially during solution processing, gives rise to ionic defects and leads to p-type self-doping.^[11] Second, the fast

1. Introduction

Organic–inorganic halide perovskites have attracted extensive interest in solar cells and light-emitting diodes over the last decade due to their favorable optoelectronic properties and

S. Wang, K. Bidinakis, C. Haese, F. H. Hasenburg, O. Yildiz, Z. Ling, R. Graf, P. W. M. Blom, S. A. L. Weber, W. Pisula, T. Marszalek
Max Planck Institute for Polymer Research
Ackermannweg 10, 55128 Mainz, Germany
E-mail: pisula@mpip-mainz.mpg.de; marszalek@mpip-mainz.mpg.de

The ORCID identification number(s) for the author(s) of this article can be found under <https://doi.org/10.1002/sml.202207426>.

© 2023 The Authors. Small published by Wiley-VCH GmbH. This is an open access article under the terms of the Creative Commons Attribution-NonCommercial License, which permits use, distribution and reproduction in any medium, provided the original work is properly cited and is not used for commercial purposes.

S. Frisch, M. Kivala
Organisch-Chemisches Institut
Ruprecht-Karls-Universität Heidelberg
Im Neuenheimer Feld 270, 69120 Heidelberg, Germany

S. A. L. Weber
Institute of Physics
Johannes Gutenberg University Mainz
Duesbergweg 10-14, 55128 Mainz, Germany

W. Pisula, T. Marszalek
Department of Molecular Physics
Faculty of Chemistry
Lodz University of Technology
Zeromskiego 116, Lodz 90-924, Poland

DOI: 10.1002/sml.202207426

crystallization rate of Sn-based perovskites as compared to Pb counterparts results in poor film morphology and low surface coverage.^[12] Therefore, controlling the crystallization and oxidation to reduce defects and charge traps is crucial in suppressing ion migration and maximizing the charge carrier transport in 2D Sn-perovskite films with respect to the ultimate FET performance.

To date, several approaches, involving solvent and precursor engineering,^[13] 2D/3D structure,^[14] and metallic iodide doping,^[15] have been proposed to address the above limitations and present promising improvements in 2D Sn-based perovskite FET devices. Recently, we introduced hot-cast 2-thiopheneethylammonium tin iodide ((TEA)₂SnI₄) perovskite thin films to control the film crystallization and morphology. The increased grain size resulted in an overall enhanced FET performance with pronounced gate modulation.^[16] As an alternative strategy, introducing additives into the precursor solution has been demonstrated to be an effective and facile method in modulating perovskite crystallization, passivating defects, and improving charge transport in solar cells.^[17–19] Inspired by the recent breakthroughs in Sn-based perovskite solar cells through additive engineering, various additives for FET applications, including nanotubes and polymers, have been proposed to optimize the transistor performance.^[20,21] However, a deep understanding of the influence of additives on the crystallization process of perovskites is still missing, which prevents the further rational design of additive molecules for perovskites FETs.

In this work, we propose a simple and effective additive engineering strategy via the incorporation of a pentanoic acid (PA) molecule with a carboxylic group into the perovskite precursor solution. The effects of PA on the passivation of defects, film formation, crystallinity, and device performance of 2D (TEA)₂SnI₄-based FETs are systematically investigated. It is demonstrated that PA interacts with TEAI and [SnI₆]^{4–} through hydrogen and coordination bonding effectively improving crystallinity, enlarging grain size, and reducing defect density. Kelvin probe force microscopy (KPFM) measurement further confirms the additive effect and the origin of the improvement in FET performance. As a result, the p-channel (TEA)₂SnI₄ transistors exhibit increased charge carrier mobility at room temperature from 0.2 cm² V^{–1} s^{–1} of

the control device to 0.7 cm² V^{–1} s^{–1} with additive treatment. At a low temperature of 100 K, the mobility further rises to 2.3 cm² V^{–1} s^{–1} along with reduced dual-sweep hysteresis.

2. Results and Discussion

The chemical structures of organic spacer TEA and additive PA are shown in Figure 1a. Liquid-state ¹H and ¹¹⁹Sn nuclear magnetic resonance (NMR) spectroscopy is performed in order to understand and identify the interaction between PA and perovskite precursors TEAI and SnI₂. Different contents of PA are used from 0, 0.25, 0.5, 0.75, to 1 vol% in the precursor solution. The preparation details of the precursor solution are described in the Experimental Section. First, a plain PA solution without the perovskite precursors is probed and the result is shown in Figure S1, Supporting Information. The resonance signal with a ¹H chemical shift at 11.9 parts per million (ppm) can be attributed to the active hydrogen in the carboxylic group of PA. Then PA is added as an additive at various volumes to the TEAI precursor deuterated dimethyl sulfoxide-*d*₆ (DMSO-*d*₆) solution. In the ¹H NMR spectra for the PA+TEAI mix solution, the gradual emerging of the PA signal is observed with its higher concentration indicating the formation of O=C–OH...I[–] hydrogen bonding with a significant exchange dynamic. In addition, ¹¹⁹Sn NMR spectra are analyzed after the addition of PA to the SnI₂ solution at different concentrations (Figure S2, Supporting Information). Figure 1b shows the ¹¹⁹Sn chemical shift as a function of the PA volume ratio. The observed down-field shift of the ¹¹⁹Sn signal with increasing PA concentration can be explained by the electronic deshielding of the Sn²⁺ ion during its coordination bonding to the oxygen of PA in the form of HO–C=O...Sn²⁺.^[22] From these results, it can be concluded that PA undergoes hydrogen and coordination bonding by the carboxylic group with iodide and tin atoms of the precursors (Figure 1c).

To verify the influence of the PA additive on the surface morphology of the perovskite films, atomic force microscopy (AFM) measurement is employed for pristine and PA-modified (TEA)₂SnI₄ films deposited on a silicon/silicon dioxide wafer, and the corresponding results are shown in Figure 2a–e. The

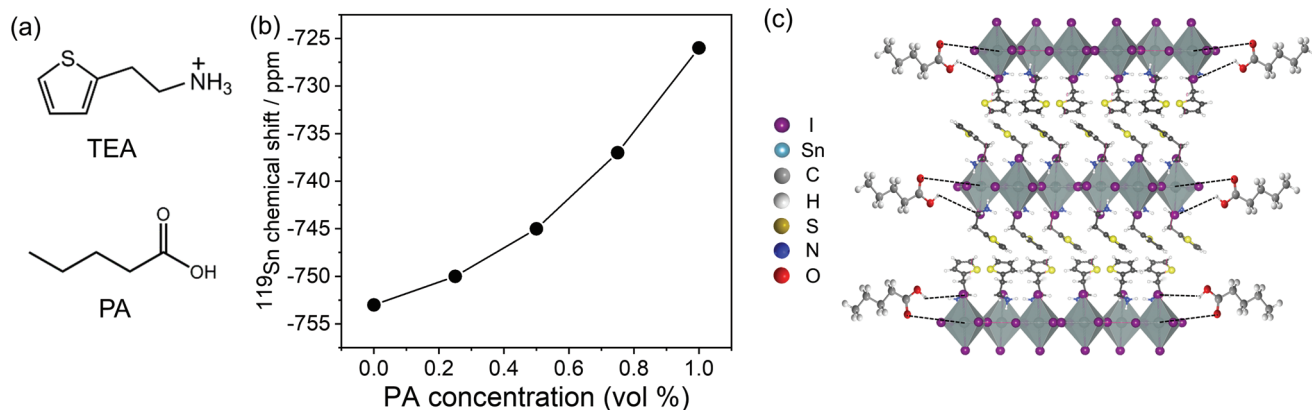


Figure 1. a) Chemical structures of organic spacer TEA and additive PA. b) ¹¹⁹Sn chemical shift as a function of the PA volume ratio. c) Representation of hydrogen bonding (C–OH...I) and coordination bonding (C=O...Sn) between PA and (TEA)₂SnI₄.

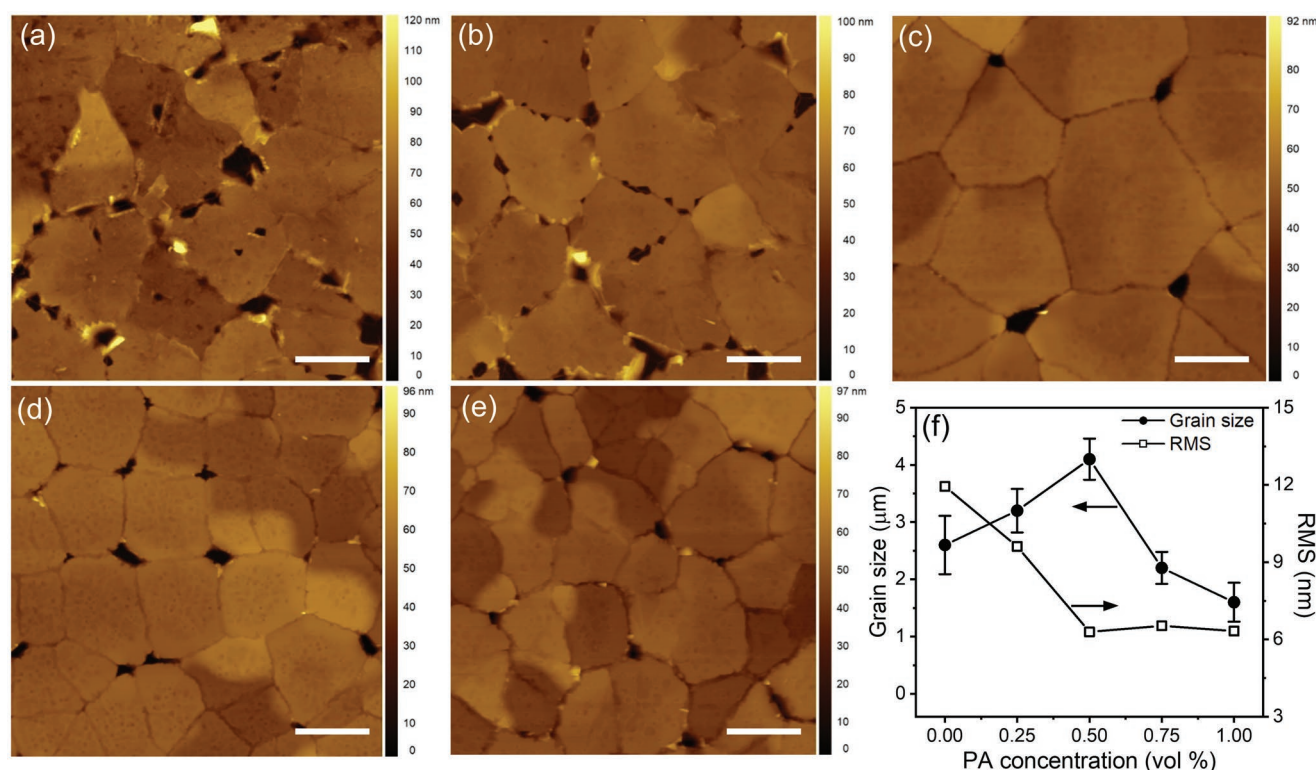


Figure 2. AFM height images of (TEA)₂SnI₄ films with PA at the concentration of a) 0 vol%; b) 0.25 vol%; c) 0.5 vol%; d) 0.75 vol%; and e) 1 vol%. Scale bar in all images is 2 μm. f) Grain size distribution and surface roughness of (TEA)₂SnI₄ films as a function of PA concentration.

control film without additives exhibits a small grain size as confirmed by the literature.^[23] Inferior film morphology and poor film coverage with numerous inevitably unfavorable pinholes appear due to the fast crystallization, which is a typical drawback for tin-based perovskites.^[24] Upon addition of PA to the (TEA)₂SnI₄ precursor solution, smoother and more homogeneous films with less pinholes are obtained. Furthermore, the grain size increases to around 4 μm at a PA concentration of 0.5 vol%. The dependence of the grain size on PA concentration is shown in Figure 2f. We postulate that the strong interaction between the PA additive and the precursors initiates heterogeneous nucleation centers inducing crystal growth preferentially at these nucleation sites, which induces the growth of perovskite grains with high surface coverage.^[25] In addition, the perovskite film with 0.5 vol% PA exhibits a much smaller surface roughness with a root-mean-square (RMS) value of 6.3 nm in comparison to 11.9 nm for the pristine sample. A smoother film surface is beneficial for the contact between the electrodes and perovskite film in the FET facilitating carrier injection and extraction.^[26] Indeed there are still small pinholes in the film with 0.5 vol% PA. However, their size and density are significantly reduced in comparison to the pristine (TEA)₂SnI₄ film and further optimization of the crystallization process will be performed in the future. The RMS values for all perovskite films are summarized in Figure 2f. At higher PA levels between 0.5 and 1 vol%, the grain size clearly decreases compared with the pristine sample, probably due to an excessive formation of heterogeneous nucleation sites in the precursor solution.^[27] The results demonstrate that the PA additive effectively tunes

the crystallization process and improves film morphology, including the surface roughness and grain size, which is expected to enhance the electronic properties of the perovskite films in FET devices.

Based on the above AFM results, we choose the PA concentration of 0.5 vol% as an optimum to investigate the impact of the additive on the crystal structure and molecular organization of the (TEA)₂SnI₄ films by X-ray diffraction (XRD) and grazing incidence wide-angle X-ray scattering (GIWAXS) measurements. Figure 3a shows the XRD patterns of the corresponding two (TEA)₂SnI₄ films without and with 0.5 vol% PA. The two samples exhibit the typical (00*l*) out-of-plane organization (*l* = 2, 4, 6, 8, 10, and 12) indicating a layered structure.^[28] Both films show the same position for the (002) diffraction peak at 5.68°, while the calculated interlayer spacing *D*₀₀₂ is 15.6 Å. These results prove that the PA additive does not cause any disruption of the out-of-plane lattice in the layered perovskite structure. The films with 0.5 vol% PA additive exhibit substantially increased intensities of the main diffraction peaks compared with the pristine film, although the two films have the same thickness. In addition, the corresponding full width at half maximum (FWHM) values are extracted to be 0.23° and 0.21°, respectively, suggesting slightly improved out-of-plane crystallinity of the film with PA. GIWAXS measurements are further executed to understand the contribution of the PA additive on the molecular organization. The crystal coherence lengths in the (002) direction calculated from the Scherrer equation are 197 nm for pristine and 236 nm for the optimized (TEA)₂SnI₄ film as shown in Figure 3b,c. Higher order reflections,

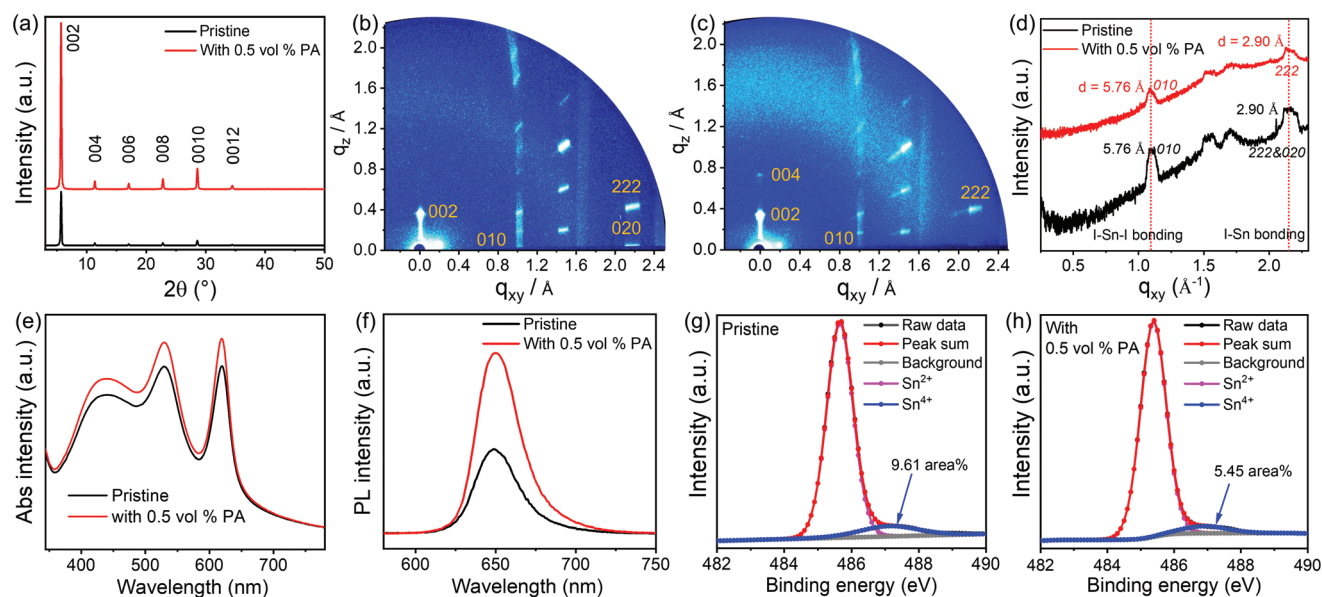


Figure 3. a) XRD and b,c) GIWAXS patterns (main reflections are assigned by Miller indices) for pristine and PA containing (TEA)₂SnI₄ films; d) in-plane profiles of both GIWAXS patterns; e) UV-vis absorption and f) photoluminescence spectra; XPS spectra of Sn 3d for (TEA)₂SnI₄ films prepared without (g) and with (h) PA. The peak fitting indicates the ratio changes of Sn⁴⁺ upon PA addition.

including (004), are observed in the film with PA indicating a long-range organization of crystal structures in the out-of-plane direction of the film, further confirming the XRD results. From the out-of-plane position of the (00*l*) reflections, it is possible to conclude that the inorganic part [SnI₆]^{4−} is organized parallel to the substrate, which is favorable for the in-plane charge carrier transport in FETs.^[29] The in-plane integration of the peak intensity for q_{xy} from 0° to 15° is shown in Figure 3d. The in-plane (010) and (020) reflections are attributed to Sn–I and I–Sn–I bonds with corresponding d-spacings of 2.9 and 5.8 Å, which agree well with the literature.^[30] However, the (020) reflection is missing for the film with PA additive compared to the pristine (TEA)₂SnI₄ film, probably due to the strong interaction between PA and the inorganic [SnI₆]^{4−} framework.

To evaluate the impact of the PA additive on the optoelectronic properties of the (TEA)₂SnI₄ films, we acquired UV-vis absorption (Abs) and steady-state photoluminescence (PL) spectra of pristine and films with 0.5 vol% PA, as shown in Figure 3e,f. In the absorption spectra, both (TEA)₂SnI₄ films without and with 0.5 vol% PA show three peaks at 440, 529, and 619 nm, where the sharp absorption peak at 619 nm can be attributed to the intrinsic exciton absorption in the crystal lattice. The film with 0.5 vol% PA exhibits slightly stronger absorption than the pristine one. Similar behavior is observed in the PL spectra. The stronger PL intensity for the film with 0.5 vol% PA in comparison to the pristine sample indicates a reduced number of defects within the optimized perovskite layer.^[31] X-ray photoelectron spectra (XPS) measurements were further used to identify the existence of PA additive and Sn²⁺ oxidation for pristine and 0.5 vol% PA-based (TEA)₂SnI₄ films. The Sn 3d XPS spectra confirm that Sn from (TEA)₂SnI₄ is the active site to coordinate with the O=C–OH units in PA since the peak exhibits a shift toward lower binding energy from pristine to PA added (TEA)₂SnI₄ films (Figure 3g,h). More impor-

tantly, a reduced proportion of Sn⁴⁺ from 9.61 atomic% for the pristine sample to 5.45 atomic% for the PA-based (TEA)₂SnI₄ film is also observed. Since Sn²⁺ is prone to be oxidized to the Sn⁴⁺ ionic defect which can occur either in precursor solution and/or during film formation processing. Therefore, minimizing the Sn⁴⁺ valence state is desirable to reduce the trap density and prolong the carrier diffusion length in the film.^[32] From the XPS results, we conclude that the PA additive can effectively passivate defects through strong retardation of Sn²⁺ oxidation. Additionally, we analyzed the XPS wide spectra in-depth for pristine and optimized PA-added (TEA)₂SnI₄ films (Figure S3a, Supporting Information). As the PA additive contains carbon and oxygen elements, we compare the XPS peaks of C 1s and O 1s for pristine and PA-based (TEA)₂SnI₄ films. From elemental analysis, we find a distinct shoulder peak for C 1s at 285.2 eV (Figure S3b, Supporting Information) and an overall increased amount of C concentration for the (TEA)₂SnI₄ film with PA additive. For O 1s, we find a dominant peak at 532 eV, which can be assigned to C–OH and C–O–C groups (Figure S3c, Supporting Information). Therefore, combined with the above analysis, we can conclude that the PA additive is successfully incorporated into the perovskite film.

To study the effect of PA on the electrical properties of the (TEA)₂SnI₄ semiconducting film and determine the optimum concentration of PA in the perovskite films regarding the device performance, FETs with a bottom-gate top-contact geometry were fabricated, as shown in Figure 4a. The transfer characteristics were recorded at $V_{ds} = -60$ V with V_g scanned from +60 to −60 V in pulse mode (see more details in the Experimental Section). Figure 4b,c shows the statistics of the charge carrier mobility and hysteresis (V_g difference at $|I_{ds}| = 10^{-7}$ A of both sweeping directions) in the transfer characteristics as a function of the PA concentration at 295 K. The mobility is extracted from the saturation region of the transfer curve in a forward

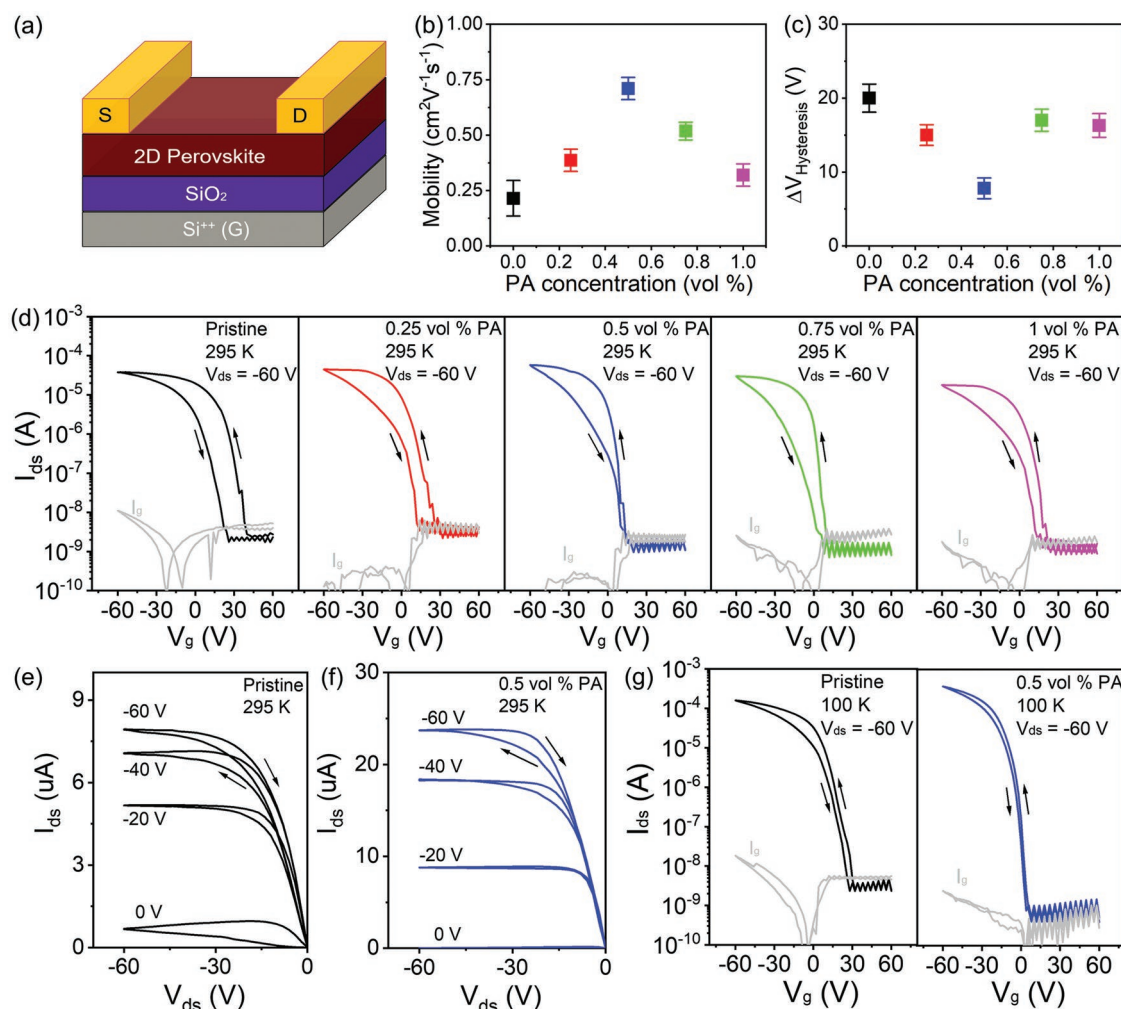


Figure 4. a) Device structure of $(\text{TEA})_2\text{SnI}_4$ FETs. b) Charge carrier mobility and c) hysteresis width of $(\text{TEA})_2\text{SnI}_4$ FETs with different PA concentrations. Error bars present standard deviation calculated from 12 devices per type. d) Transfer characteristics at 295 K (I_g is the gate leakage current). Corresponding output characteristics of pristine (e) and PA-based (at 0.5 vol%) devices (f) at 295 K. g) Transfer characteristics of pristine and modified devices with PA concentration of 0.5 vol% at 100 K. Arrows indicate the direction of the sweeps.

direction. The pristine $(\text{TEA})_2\text{SnI}_4$ FET reveals p-channel FET characteristics with an average hole mobility (μ_h) of $0.2 \text{ cm}^2 \text{ V}^{-1} \text{ s}^{-1}$, a subthreshold swing (SS) of 5 V dec^{-1} , an on/off current ratio ($I_{\text{on/off}}$) of 1.5×10^4 , and a threshold voltage (V_{th}) of 33 V (Figure S4, Supporting Information). The FETs based on the additive PA at various concentrations exhibit markedly improved overall performance. Notably, the device with 0.5 vol% PA demonstrates the best performance. At the optimal PA concentration of 0.5 vol%, the maximum channel current in the transfer curve corresponds to a smaller SS value of 2.9 V dec^{-1} , a charge carrier mobility of $0.7 \text{ cm}^2 \text{ V}^{-1} \text{ s}^{-1}$, an $I_{\text{on/off}}$ of 6.1×10^4 , and a V_{th} of 9 V, representing a remarkable improvement in the transistor performance (Table S1, Supporting Information). In our device with PA additive, the V_{th} values are significantly reduced compared to the pristine FET demonstrating that the PA additive effectively eliminates defects. However, V_{th} increases for a higher concentration of PA possibly due to the insulating nature of the PA additive, reduced grain size, and increased number of grain boundaries. Based on the repeated

measurements of a large number of devices, the device performance is confirmed to be highly reliable and reproducible with a small standard deviation of $\pm 0.053 \text{ cm}^2 \text{ V}^{-1} \text{ s}^{-1}$. The trap density (N_t) at the dielectric/perovskite interface with the whole channel area of $80 \mu\text{m} \times 1000 \mu\text{m}$ is calculated using SS values as defined by the following equation^[33]

$$SS = \frac{k_B T \ln 10}{q} \left[1 + \frac{q^2}{C_i} N_t \right] \quad (1)$$

with k_B the Boltzmann constant; T the absolute temperature; q the elementary charge; and C_i the areal capacitance of the dielectric layer. Accordingly, N_t decreases from $6.1 \times 10^{12} \text{ cm}^{-2} \text{ eV}^{-1}$ for the pristine FET to $3.5 \times 10^{12} \text{ cm}^{-2} \text{ eV}^{-1}$ for the 0.5 vol% PA-based FET, as shown in Figure S5, Supporting Information. However, when the PA concentration is further increased to 1 vol%, the trap density N_t rises again to $5.6 \times 10^{12} \text{ cm}^{-2} \text{ eV}^{-1}$, which can be ascribed to the decreased grain size leading to a high density of grain boundaries. These results suggest that

the additive at optimal concentration improves the film quality at the perovskite/dielectric interface contributing to lower SS and reduced trap density. When the PA concentration is further increased, a declined device performance is observed. The PA concentration of 1 vol% leads to a decreased mobility of $0.3 \text{ cm}^2 \text{ V}^{-1} \text{ s}^{-1}$, as shown in Figure 4d. The above results reveal an optimum PA concentration to achieve the highest device performance. At a too-high concentration, the insulating properties of the additive and reduced grain size possibly result in poor charge transport.^[34] The output characteristics of the optimal device at 295 K in Figure 4f are significantly improved compared to the pristine device in Figure 4e, which shows a weak gate modulation of the current. These observations further confirm the beneficial effect of PA on the electronic properties of $(\text{TEA})_2\text{SnI}_4$ FETs and more details on the charge transport are discussed below. It is worth noting that the hysteresis directions of the output and transfer curves are opposite. Perovskite-based transistors exhibit gradually expanded hysteresis when the bias sweep rate changes in the presence of ion migration.^[20] For this reason, the transfer characteristics were recorded by using pulse mode to eliminate this effect. Nevertheless, V_{DS} in the output characteristics is changed in sweep mode. The sweep range of the output curve is from 0 to -60 V and then back from -60 to 0 V . These are the typical measurement modes for perovskite transistors.^[35] We assume that due to the sweeping mode, the polarization of the source and drain area occurs which results in clockwise hysteresis in the output characteristics. However, this aspect will be studied in more detail in the future. The corresponding output characteristics of the device with other PA concentrations are shown in Figure S6, Supporting Information. Photoelectron yield spectra were performed to analyze the electronic structure of pristine and optimized 0.5 vol% PA-based $(\text{TEA})_2\text{SnI}_4$. As shown in Figure S7, Supporting Information, the valence-band maximum (VBM) values are determined to be 5.18 and 5.23 eV, respectively. This indicates that the PA additive has negligible impact on the charge injection barrier at Au/perovskite interface in the FET devices.^[36]

In addition to higher mobilities, the FETs based on $(\text{TEA})_2\text{SnI}_4$ with PA also exhibit reduced dual-sweep hysteresis. To quantitatively analyze the hysteresis for the FET devices operating at room temperature, the width of the hysteresis for V_g (ΔV) in the forward and backward direction is calculated at $|I_{\text{ds}}| = 10^{-7} \text{ A}$, which is around halfway between the on and off states.^[37,38] The pristine devices demonstrate a large ΔV of 19 V, which decreases to 8 V at the optimized PA concentration of 0.5 vol%. The lowered hysteresis is attributed to the strong interaction between PA and precursors which passivates defects, increases the grain size, and inhibits ion migration in the film. We notice that the optimized device with 0.5 vol% PA additive still exhibits gate voltage-dependent hysteresis in the transfer characteristics. When positive (negative) ions drift toward (away from) the interface under a negative gate voltage, the accumulation of these mobile ions shields the applied gate field and reduces the concentration of holes in the accumulation layer of the FET. The larger negative V_g significantly increases the number of accumulated ions and strengthens the screening of the gate voltage.^[20] At higher gate bias in the saturation region, we assume that all mobile ions are accumulated at the perovskite/dielectric interface. In this case, further

increasing the gate voltage has only negligible influence on the screening effect but increases the number of charge carriers, resulting in a lower hysteresis. The hysteresis in metal halide perovskite transistors is generally believed to originate from ion migration and interface traps. The hysteresis induced by mobile ions is strongly dependent on the presence of defects in the perovskite films.^[14] The enlarged grain size is also beneficial for the device's performance due to the reduced grain boundaries which act as trap centers for charge carriers and pathways for ions in the perovskite film, as confirmed by our previous work.^[16] Iodide vacancies are believed as main ionic defects in the solution-processed tin halide polycrystalline perovskite thin films due to their low formation energy during film processing.^[39] In 2D $(\text{TEA})_2\text{SnI}_4$ FETs, the spacer cation TEA is stable because of its large molecular size, so iodine anions are considered to be the dominant undesired mobile ions. The lateral mobile ions accumulate at the electrode/semiconductor interface in the channel and create a built-in electric field opposite to the externally applied V_{ds} , which seriously retards the in-plane charge carrier transport in the FET.^[40] Due to the strong hydrogen and coordination bonding between PA and source materials, the density of defect-associated mobile ions is significantly suppressed accompanied by enlarged grain size, greatly improving charge transport, and reducing ion migration in the device during operation.

To further confirm the reduction of the defect density by PA treatment, we investigate the FET characteristics of pristine and PA-treated films at a low temperature of 100 K. Figure 4g shows the transfer characteristics of the pristine and optimized devices. The device with PA additive exhibits a high average μ_{h} of $2.3 \text{ cm}^2 \text{ V}^{-1} \text{ s}^{-1}$ at 100 K. The devices with other PA concentrations (0.25, 0.75, and 1 vol% PA) expose also higher mobilities at low temperatures in comparison to 295 K (Figures S8 and S9, Supporting Information). The movement of ions is commonly significantly inhibited at low temperatures. As the temperature decreases to 100 K, all devices show a reduced hysteresis compared with 295 K. This suggests that the mobile ions significantly contribute to the FET hysteresis at 295 K since it is generally believed that ion migration is drastically inhibited at low temperatures. Nevertheless, even greatly suppressed, hysteresis can be still observed at 100 K. The residual hysteresis at 100 K can be attributed to traps at the dielectric/perovskite interface.^[41] In addition, we also have calculated the interface trap densities (N_{t}) for devices operating at 100 K based on the SS values extracted from transfer curves in a forward direction. All devices show lower N_{t} values at 100 K than at 295 K, which are 5.8×10^{12} , 5.4×10^{12} , 2.7×10^{12} , 2.9×10^{12} , and $3.3 \times 10^{12} \text{ cm}^{-2} \text{ eV}^{-1}$, for the PA concentrations of 0, 0.25%, 0.5%, 0.75%, and 1%, respectively. The slightly increased interface trap densities (N_{t}) with higher PA concentration can be attributed to the moderately decreased grain size. It clearly shows that the N_{t} values are reduced with the PA concentration, further confirming that the strong hydrogen and coordination bonding between PA additive and precursor materials can effectively passivate the defects in the film and consequently improve the quality of the dielectric/perovskite interface. These results are in line with the drastically suppressed hysteresis in the output curves at 100 K. It should be pointed out that the output curve at 100 K shows a sublinear region at a small V_{ds} ,

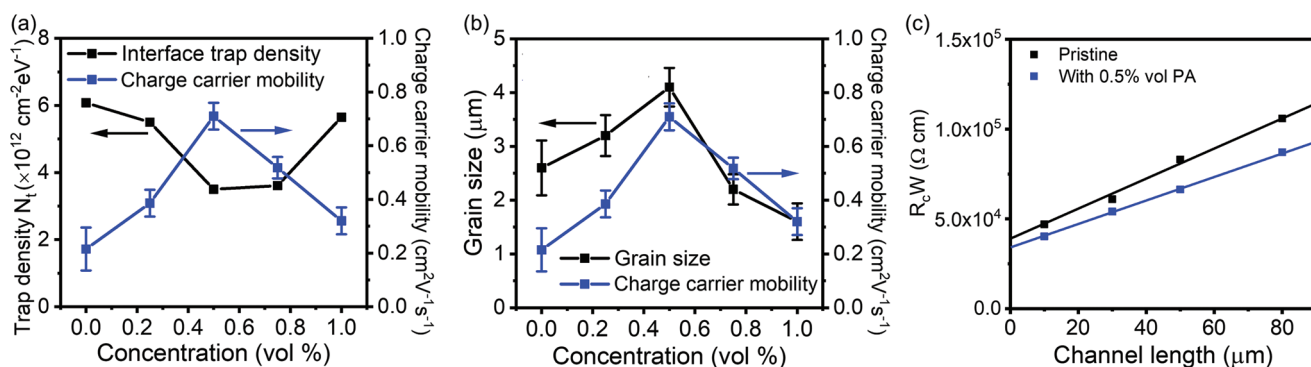


Figure 5. a) Correlation between interface trap density and charge carrier mobility and the corresponding b) correlation between grain size and charge carrier mobility for $(\text{TEA})_2\text{SnI}_4$ FETs processed with different PA concentrations. c) Transmission-line method with $R_C W$ as a function of channel length for pristine and optimal 0.5 vol% PA-based $(\text{TEA})_2\text{SnI}_4$ perovskite FETs at 295 K. The contact resistance is determined from the y-axis intercept. The drain current was collected from the linear region at $V_g = -60 \text{ V}$ and $V_{ds} = -6 \text{ V}$.

which indicates contact resistance in the device. The effect of stationary ions cannot be neglected and they might contribute to the remaining contact resistance.^[42,43] Through optimization of the contact resistance and/or the choice of optimized interlayers, some improvements in performance are expected to be achieved in the future.

We have then checked the correlation between the interface trap density and field-effect mobility for different PA concentrations at 295 K. **Figure 5a** reveals a clear correlation between trap density and mobility. The charge carrier mobility increases with lower interface trap density. On the contrary, the grain size is not closely linked to the charge carrier mobility as presented in **Figure 5b**, although both parameters exhibit similar trends with differences regarding the concentration of PA additive (**Figure S10**, Supporting Information). For example, the pristine film shows a grain size of around $2.6 \mu\text{m}$, which is much larger than that of $1.6 \mu\text{m}$ in the film with the highest PA concentration of 1 vol%. However, the corresponding pristine device results in lower mobility. Additionally, $(\text{TEA})_2\text{SnI}_4$ film without and 0.75 vol% PA exhibit similar grain sizes of around 2.6 and $2.2 \mu\text{m}$, respectively. Nevertheless, the pristine $(\text{TEA})_2\text{SnI}_4$ FET leads to a charge carrier mobility of $0.2 \text{ cm}^2 \text{ V}^{-1} \text{ s}^{-1}$. This is significantly lower than the mobility of $0.52 \text{ cm}^2 \text{ V}^{-1} \text{ s}^{-1}$ for the device with 0.75 vol% PA. Therefore, the above discussion further confirms that the superior FET performance for $(\text{TEA})_2\text{SnI}_4$ films with optimized PA concentration can be ascribed to two factors: defect passivation by suppressing Sn^{2+} oxidation and improved film morphology. Both of these effects synergistically result in improved charge carrier transport and inhibited ion migration.

We examined the influence of PA additives on contact resistance ($R_C W$) in the devices through the transmission line method (TLM).^[16] As shown in **Figure 5c**, the contact resistance of $4.1 \times 10^4 \Omega \text{ cm}$ for pristine devices is reduced to $3.5 \times 10^4 \Omega \text{ cm}$ for the optimized 0.5 vol% PA-based FETs, which can be attributed to the decreased ionic defects by PA additive. The reduction of contact resistance is expected to improve the charge injection in FET devices. We have also investigated the bias stress stability for pristine and 0.5 vol% PA optimized $(\text{TEA})_2\text{SnI}_4$ FETs. **Figure S11**, Supporting Information, shows the change in source-drain current under a constant bias of $V_g = V_{ds} = -60 \text{ V}$ for 500 s. The normalized source-drain cur-

rent ($I_{ds}(t)/I_{ds}(0)$) of the pristine $(\text{TEA})_2\text{SnI}_4$ FET degrades significantly faster than the optimized device. For example, the decay time to reach 20% of the initial channel current is significantly increased from 56 to 185 s for the $(\text{TEA})_2\text{SnI}_4$ FET with 0.5 vol% PA. The above results further confirm that the PA additive plays an efficient role in improving the device stability by effectively reducing defects and inhibiting ion migration.

The above results demonstrate the beneficial effects of additive engineering on film formation and FET operation. To further investigate the microscopic origin of the improved FET performance by the addition of PA, the film morphology and the potential distribution are examined using KPFM. KPFM correlates the nanoscale sample topography with the local surface potential. With all electrodes grounded, the contact potential difference (CPD) between the tip and sample gives rise to electrostatic forces (**Figure S12a**, Supporting Information).^[44] Compensating these electrostatic forces by applying an external bias to the tip allows mapping the CPD variations. By establishing electrical connections for the source, drain, and gate electrode, we can put the FET into operating conditions and map the voltage distribution across the FET channel (**Figure S12b**, Supporting Information).^[45] In order to avoid cross-talk to the KPFM signal from accentuated topographical features at the grain boundaries, heterodyne frequency-modulation KPFM is employed, which is deemed as the most reliable KPFM method.

First, the effect of the additive in terms of the localization and passivation of defects in the perovskite film is analyzed. Since the charge carrier transport occurs laterally along the channel, defects giving rise to deep trap states within the band gap would pose a hindrance to charge flow from source to drain, and therefore, negatively affecting the transistor performance. Moreover, these energy states are expected to cause band bending leading to a change in the measured CPD at the grain boundaries. In the first step, we conducted KPFM while keeping all three FET electrodes grounded in order to map the relative work functions of the gold electrodes, perovskite grain interiors, and grain boundaries. For both the pristine (**Figure S13a**, Supporting Information) and the 0.5 vol% PA modified device (**Figure S13b**, Supporting Information), a clear increase of the CPD at the grain boundaries with respect to the grain interiors

is observed, which corresponds to energetic barriers for charge carrier movement (Figure S14, Supporting Information). A statistical analysis of ten random grain boundary CPD crests for both pictures reveals that the amount of voltage by which the CPD rises does not vary much between the two devices we measured, within experimental error (Figure S15, Supporting Information). However, we identify the superior structure in the sample treated with the PA additive in terms of a larger grain size distribution. Having larger grains along the channel path means that charge carriers migrate through less energetically unfavorable boundaries, which could explain the improved electronic characteristics of the optimized device when current flows across the channel.

To investigate the advantage of the optimized morphology with additive engineering in transistors, KPFM measurements on pristine and modified devices under operating conditions are conducted (Figure 6a,c). Specifically, a voltage of -9 V is applied on the drain, while keeping the source grounded, which corresponded to the output characteristics (Figure 4e,f) in the linear regime. Additionally, a voltage of -44 V is applied to the gate accordingly, which exceeded the threshold voltage from the transfer characteristics in Figure 4d and corresponded to a conductive channel. In the case of the pristine device, we notice from Figure 6a,b that the potential decreases from source to drain in a stepwise manner. The large voltage drops correspond to resistive barriers to charge carrier flow, which seem to be more pronounced on certain grain boundaries. Previous studies on perovskite solar cells and FETs have linked this behavior to a pronounced ion migration and accumulation inside the perovskite film.^[46] The extent to which ionic accumulation obstructs electronic charge carrier flow can be explained through simple electrostatics. We propose that the high density of ionic defects in the pristine device leads to an accentuated ion drift due to the source-drain voltage and hence ionic accu-

mulation close to the electrode/semiconductor interfaces. This screens the applied electric field, thus inhibiting the charge flow required for device operation, as mentioned earlier. Since electrostatic fields are conservative, they relate to their corresponding electrical potential as $E = -\nabla V$, or in 1D as $E = -\frac{dV}{dx}$.

For the calculation of the electric field in the pristine device due to ion migration, the adjacent-averaging smoothing method is employed for the potential plot, in order to avoid artifacts in the electric field plot because of the differentiation. The resulting plot (Figure S16, Supporting Information) reveals an electric field close to the source electrode, which partially screens the source-drain voltage and lowers the field-effect mobility values for that transistor, further confirming that iodine anions are the dominant mobile ions.^[42] On the other hand, the modified device exhibits a mostly continuous linear decline along the channel, implying that the current is only limited by the bulk lateral resistance of the perovskite film. These results once again confirm that the addition of 0.5 vol% PA to the perovskite precursor solution is beneficial for device operation, as the current flow is less governed by the energy barriers at the grain boundaries.

3. Conclusion

In this work, PA is incorporated as an additive into the precursor solution for the fabrication of high-performance 2D (TEA)₂SnI₄ FETs. We found that the PA additive effectively modifies the perovskite nucleation through the formation of hydrogen and coordination bonding. As a result, the (TEA)₂SnI₄ film with 0.5 vol% PA shows significantly suppressed Sn²⁺ oxidation, improved film morphology regarding the surface roughness and grain size, and increased crystallinity,

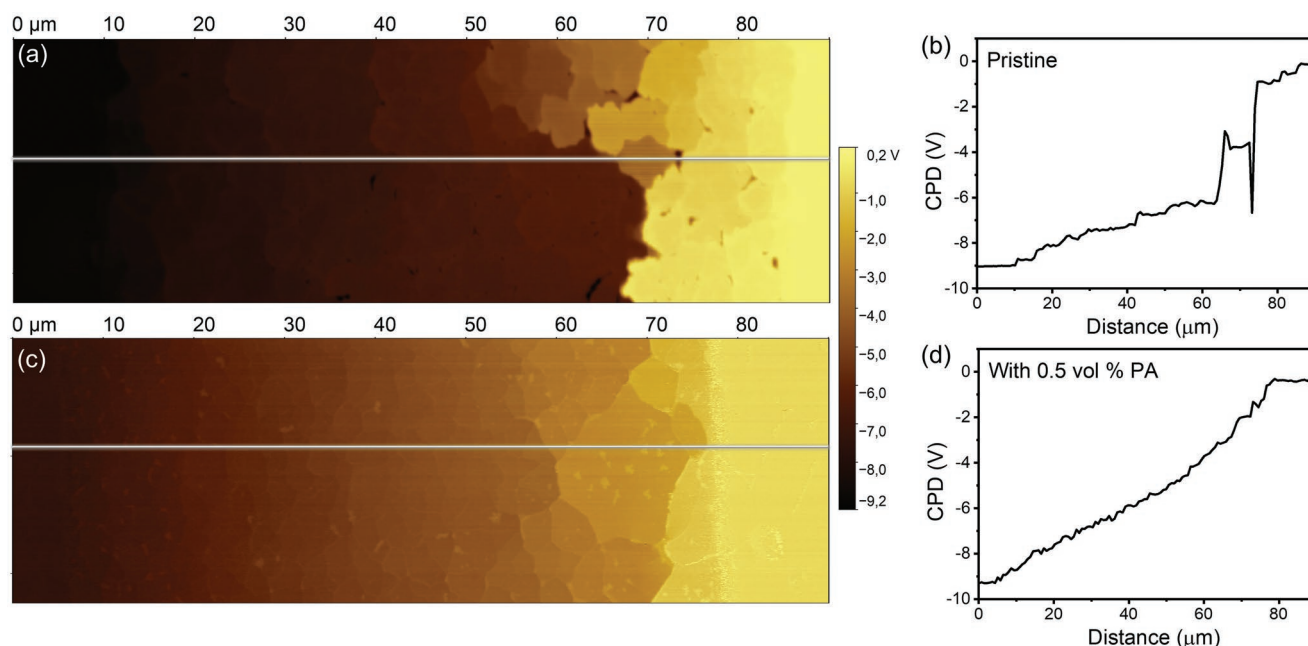


Figure 6. Potential maps and corresponding profiles of a,b) pristine and c,d) optimized FET measured with KPFM for $V_g = -44$ V and $V_{ds} = -9$ V.

which synergistically augmented the FET performance with the highest mobility of $0.7 \text{ cm}^2 \text{ V}^{-1} \text{ s}^{-1}$ at 295 K. This is a more than threefold enhancement compared to the control pristine device with $0.2 \text{ cm}^2 \text{ V}^{-1} \text{ s}^{-1}$. In addition, the ion-induced hysteresis in the transfer characteristics of the transistor is greatly inhibited and the corresponding mechanism is elucidated. Moreover, benefiting from the reduced defects and ion migration, the optimal device results in higher mobility of $2.3 \text{ cm}^2 \text{ V}^{-1} \text{ s}^{-1}$ at 100 K. These results demonstrate the important role of additive engineering in modulating the film quality and electronic properties of 2D tin halide perovskite films. Our proposed strategy provides a facile solution for the realization of high-performance tin-based perovskite FETs.

4. Experimental Section

Materials: The organic cation TEA was synthesized according to a previously reported procedure.^[16] Tin (II) iodide (99.999%), pentanoic acid solution (CAS Number: 109-52-4), and dimethylformamide (DMF) (anhydrous, 99.8%) were obtained from Sigma-Aldrich. All chemicals were used without further purification. Silicon wafers were purchased from Ossila Ltd.

Preparation of Precursor Solution: The precursor solution was obtained by mixing the precursor materials TEAI and SnI_2 at a molar ratio of 2:1 in DMF at 0.1 M concentration. For the PA-incorporated $(\text{TEA})_2\text{SnI}_4$ precursor, 0.25, 0.5, 0.75, and 1 vol% of PA were added to the pristine $(\text{TEA})_2\text{SnI}_4$ solution. The solution then was stirred overnight at 60 °C in a glovebox and cooled to room temperature before use. The as-prepared fresh precursor solution was filtered through a 0.2 μm PTFE filter before spin-coating.

Device Fabrication and Measurement: Heavily doped Si/SiO₂ wafers ($1.5 \times 2 \text{ cm}$) were used as the substrates and cleaned by sonicating in deionized water, acetone, and isopropyl, consecutively for 20 min each. After drying in nitrogen flow, the substrates were treated by UV/ozone for 20 min and then transferred into a glovebox for film deposition. This was followed by spin coating of the $(\text{TEA})_2\text{SnI}_4$ perovskite semiconductor layer at 4000 rpm for 60 s and subsequent annealing at 100 °C for 10 min. The SiO₂ layer with a thickness of 300 nm was adopted as a dielectric layer. Finally, 80 nm gold source and drain electrodes were deposited by thermal evaporation through a shadow mask to construct $80 \times 1000 \mu\text{m}$ (length \times width) transistor channels. The device characterization was performed using a semiconductor parameter analyzer (Keithley 4200-SCS) in a vacuum (10^{-6} mbar) to avoid degradation. The transfer characteristics were recorded in pulse mode, and the output characteristics were measured in continuous mode. In the pulse mode, V_g was applied over a short impulse of 1 s. The temperature-dependent measurements were performed using a Desert Cryogenics low-temperature probe station. Mobility values of FETs were extracted with the following equation^[47]

$$\mu = \frac{2L}{WC_i} \left(\frac{\partial \sqrt{I_{ds}}}{\partial V_g} \right)^2 \quad (2)$$

where L , W , and C_i are the channel length and width and the unit capacitance of the oxide dielectric, respectively.

Film Characterization: Solution NMR experiments were performed on a Bruker Avance 400 MHz spectrometer equipped with a BBI probehead with z-gradients. ¹H spectra were acquired using 32 scans and a recycle delay of 2 s. ¹¹⁹Sn spectra were acquired using 256 scans and a recycle delay of 10 s. d₆-DMSO from the company Deutero GmbH was used as a solvent without further purification. All NMR experiments were performed under ambient conditions. The thin film morphology was characterized by a Bruker Dimension Icon FS AFM in tapping mode at room temperature. GIWAXS measurements were

performed by means of a solid anode X-ray tube (Siemens Kristalloflex X-ray source, copper anode X-ray tube operated at 35 kV and 20 mA), Osmic confocal MaxFlux optics, X-ray beam with pinhole collimation, and a MAR345 image plate detector. All X-ray scattering measurements were measured under a vacuum ($\approx 1 \text{ mbar}$) to reduce air scattering and prevent degradation of the sample. All data processing and analysis were performed using the software package Data squeeze. The thin film XRD patterns were recorded in the 2θ between 3° and 50°, with a step of 0.01° and a speed of 10 degrees per minute, using a Rigaku D/MAX 2600 V with Cu K α ($\lambda = 1.5406 \text{ \AA}$) radiation. The interlayer distance was calculated by Bragg's law $2d \sin \theta = n\lambda$, where λ is the X-ray wavelength, 1.5406 Å; θ is the Bragg angle of the diffraction peak, and $n = 2$, respectively. XPS measurements were conducted by using a PHI 5500 Multi-technique System with a base pressure of $\approx 10^{-9}$ torr. The X-ray radiation was Al K α emission (1486.7 eV; take-off angle, 75°). Thin film absorption spectra were recorded on an Agilent UV-vis-NIR Cary-5000 spectrometer in transmission mode. Spectra were collected in the range of 300–800 nm. PL measurements were conducted using a high-resolution monochromator and hybrid photomultiplier detector (PMA Hybrid 40, PicoQuant GmbH). For the photoelectron yield measurements, the thin films were coated on conductive Si substrates. Then the valence band minimum was evaluated with a photoelectron spectrometer (AC-2S LC) by RIKEN KEIKI CO., LTD. The spectra were recorded for three samples to confirm the reproducibility of the measurement.

Kelvin Probe Force Microscopy Measurement: Mapping of the FET potential distribution was performed via KPFM, using an Asylum Research MFP3D Microscope (Oxford Instruments) together with a lock-in amplifier (HF2LI-MOD, Zurich Instruments). To avoid degradation of the perovskite film, the setup was placed in an argon-filled glovebox with an atmosphere containing less than 1 ppm O₂ and minimal humidity. The sample holder allowed to establish an electrical connection to the source, drain, and gate electrodes and ground them, or apply direct current voltages to them individually. Due to the limitation of the setup, the auxiliary output channels of the HF2 lock-in amplifier was used and applied a maximum source and drain voltage of -9 V . To generate the gate voltage, a -44 V battery stack was used with resonance frequency $\omega_0 \approx 75 \text{ Hz}$ and spring constant $\approx 3 \text{ N m}^{-1}$. The scan rate of the measurements was 0.2 Hz. To obtain reliable data, frequency modulation KPFM was employed in the heterodyne configuration, whereby the cantilever was mechanically excited at its first resonance, ω_0 , and electrically excited with an amplitude of 1 V at its second resonance minus the first $(\omega_1 - \omega_0)$.^[48] Frequency mixing between the mechanical motion and the periodic electrostatic force generated a sideband signal on the second resonance frequency, ω_1 , that was used as an input signal for the KPFM feedback.

Supporting Information

Supporting Information is available from the Wiley Online Library or from the author.

Acknowledgements

S.W. thanks the China Scholarship Council for financial support. T.M. acknowledges the Foundation for Polish Science financed by the European Union under the European Regional Development Fund (POIR.04.04.00-00-3ED8/17).

Open access funding enabled and organized by Projekt DEAL.

Conflict of Interest

The authors declare no conflict of interest.

Author Contributions

S.A.L.W. conceived the idea and designed the experiment; T.M. and W.P. supervised the study; K.B. and F.H.H. performed KPFM measurement and analyzed the data with support from S.W.; C.H. conducted the solution NMR measurement and analyzed the data with support from R.G.; O.Y. and Z.L. carried out GIWAXS measurement and data analysis under the supervision of T.M.; S.F. synthesized the organic cations under the supervision of M.K.; P.W.M.B. coordinated the work. S.A.L.W. prepared the manuscript with support from all co-authors. All authors discussed the results and contributed to this work.

Data Availability Statement

The data that support the findings of this study are available from the corresponding author upon reasonable request.

Keywords

2D lead-free perovskite transistors, additive engineering, grain engineering, ion migration

Received: November 28, 2022

Revised: February 17, 2023

Published online: March 12, 2023

- [1] S. A. Veldhuis, P. P. Boix, N. Yantara, M. Li, T. C. Sum, N. Mathews, S. G. Mhaisalkar, *Adv. Mater.* **2016**, *28*, 6804.
- [2] W. J. Yin, J. H. Yang, J. Kang, Y. Yan, S. H. Wei, *J. Mater. Chem. A* **2015**, *3*, 8926.
- [3] X. Liu, D. Yu, X. Song, H. Zeng, *Small* **2018**, *14*, 1801460.
- [4] Y. T. Li, L. Ding, J. Z. Li, J. Kang, D. H. Li, L. Ren, T. L. Ren, *ACS Cent. Sci.* **2019**, *5*, 1857.
- [5] F. Haque, M. Mativenga, *Jpn. J. Appl. Phys.* **2020**, *59*, 081002.
- [6] S. Ma, M. Cai, T. Cheng, X. Ding, X. Shi, A. Alsaedi, S. Dai, *Sci. China Mater.* **2018**, *61*, 1257.
- [7] X. Li, J. M. Hoffman, M. G. Kanatzidis, *Chem. Rev.* **2021**, *121*, 2230.
- [8] C. R. Kagan, D. B. Mitzi, C. D. Dimitrakopoulos, *Science* **1999**, *286*, 945.
- [9] T. Matsushima, S. Hwang, A. S. Sandanayaka, C. Qin, S. Terakawa, T. Fujihara, C. Adachi, *Adv. Mater.* **2016**, *28*, 10275.
- [10] C. Qin, F. Zhang, L. Qin, X. Liu, H. Ji, L. Li, Y. Hu, Z. Lou, *Adv. Electron. Mater.* **2021**, *7*, 2100384.
- [11] A. Treglia, F. Ambrosio, S. Martani, G. Folpini, A. J. Barker, M. D. Albaqami, A. Petrozza, *Mater. Horiz.* **2022**, *9*, 1763.
- [12] J. Wang, Z. Gao, J. Yang, M. Lv, H. Chen, D. J. Xue, S. Yang, *Adv. Energy Mater.* **2021**, *11*, 2102131.
- [13] H. Zhu, A. Liu, H. Kim, J. Hong, J. Y. Go, Y. Y. Noh, *Chem. Mater.* **2020**, *33*, 1174.
- [14] H. Zhu, A. Liu, K. I. Shim, J. Hong, J. W. Han, Y. Y. Noh, *Adv. Mater.* **2020**, *32*, 2002717.
- [15] J. Kim, Y. S. Shiah, K. Sim, S. Iimura, K. Abe, M. Tsuji, H. Hosono, *Adv. Sci.* **2022**, *9*, 2104993.
- [16] S. Wang, S. Frisch, H. Zhang, O. Yildiz, M. Mandal, N. Ugur, B. Jeong, C. Ramanan, D. Andrienko, H. I. Wang, M. Bonn, P. W. M. Blom, M. Kivala, W. Pisula, T. Marszalek, *Mater. Horiz.* **2022**, *9*, 2633.
- [17] J. Y. Go, H. Zhu, Y. Reo, H. Kim, A. Liu, Y. Y. Noh, *ACS Appl. Mater. Interfaces* **2022**, *14*, 9363.
- [18] Y. Reo, H. Zhu, J. Y. Go, K. In Shim, A. Liu, T. Zou, Y. Y. Noh, *Chem. Mater.* **2021**, *33*, 2498.
- [19] F. Zhang, Q. Zhang, X. Liu, L. Qin, Y. Hu, Z. Lou, F. Teng, *J. Mater. Chem. A* **2021**, *9*, 22842.
- [20] H. Zhu, A. Liu, H. L. Luque, H. Sun, D. Ji, Y. Y. Noh, *ACS Nano* **2019**, *13*, 3971.
- [21] F. Zhang, Q. Zhang, X. Liu, Y. Hu, Z. Lou, Y. Hou, F. Teng, *ACS Appl. Mater. Interfaces* **2021**, *13*, 24272.
- [22] M. A. Ruiz-Preciado, D. J. Kubicki, A. Hofstetter, L. McGovern, M. H. Futscher, A. Ummadisingu, M. Grätzel, *J. Am. Chem. Soc.* **2020**, *142*, 1645.
- [23] Z. Zhu, X. Jiang, D. Yu, N. Yu, Z. Ning, Q. Mi, *ACS Energy Lett.* **2022**, *7*, 2079.
- [24] D. Cui, X. Liu, T. Wu, X. Lin, X. Luo, Y. Wu, L. Han, *Adv. Funct. Mater.* **2021**, *31*, 2100931.
- [25] X. Meng, Y. Li, Y. Qu, H. Chen, N. Jiang, M. Li, S. Yang, *Angew. Chem.* **2021**, *133*, 3737.
- [26] M. E. Kayesh, K. Matsuishi, R. Kaneko, S. Kazaoui, J. J. Lee, T. Noda, A. Islam, *ACS Energy Lett.* **2018**, *4*, 278.
- [27] M. Ulfa, P. Wang, J. Zhang, J. Liu, W. D. de Marcillac, L. Coolen, T. Pauporte, *ACS Appl. Mater. Interfaces* **2018**, *10*, 35118.
- [28] F. Lédée, P. Audebert, G. Trippé-Allard, L. Galmiche, D. Garrot, J. Marrot, C. Quarti, *Mater. Horiz.* **2021**, *8*, 1547.
- [29] H. Jia, H. Shi, R. Yu, H. Ma, Z. Wang, C. Zou, Z. A. Tan, *Small* **2022**, *18*, 2200036.
- [30] Y. Gao, Z. Wei, P. Yoo, E. Shi, M. Zeller, C. Zhu, L. Dou, *J. Am. Chem. Soc.* **2019**, *141*, 15577.
- [31] D. Hong, Y. Zhou, S. Wan, X. Hu, D. Xie, Y. Tian, *ACS Photonics* **2018**, *5*, 2034.
- [32] H. Liang, F. Yuan, A. Johnston, C. Gao, H. Choubisa, Y. Gao, E. H. Sargent, *Adv. Sci.* **2020**, *7*, 1903213.
- [33] F. Balestra, M. Benachir, J. Brini, G. Ghibaudo, *IEEE Trans. Electron Devices* **1990**, *37*, 2303.
- [34] M. Abdel-Shakour, T. H. Chowdhury, K. Matsuishi, I. Bedja, Y. Moritomo, A. Islam, *Sol. RRL* **2021**, *5*, 2000606.
- [35] S. P. Senanayak, M. Abdi-Jalebi, V. S. Kamboj, R. Carey, R. Shivanna, T. Tian, H. Sirringhaus, *Sci. Adv.* **2020**, *6*, eaaz4948.
- [36] Z. Wang, F. Wang, B. Zhao, S. Qu, T. Hayat, A. Alsaedi, Z. A. Tan, *J. Phys. Chem. Lett.* **2020**, *11*, 1120.
- [37] H. Zhu, A. Liu, K. I. Shim, H. Jung, T. Zou, Y. Reo, H. Kim, J. W. Han, Y. Chen, H. Y. Chu, J. H. Lim, H.-J. Kim, Y.-Y. Noh, *Nat. Commun.* **2022**, *13*, 1741.
- [38] H. Wan, Y. Cao, L. W. Lo, J. Zhao, N. Sepulveda, C. Wang, *ACS Nano* **2020**, *14*, 10402.
- [39] S. Zhao, L. Xiao, *Phys. Chem. Chem. Phys.* **2022**, *24*, 403.
- [40] F. Jiang, J. Pothoof, F. Muckel, R. Giridharagopal, J. Wang, D. S. Ginger, *ACS Energy Lett.* **2020**, *6*, 100.
- [41] I. Vladimirov, S. Müller, R. P. Baumann, T. Geßner, Z. Molla, S. Grigorian, R. T. Weitz, *Adv. Funct. Mater.* **2019**, *29*, 1807867.
- [42] F. Liu, L. Wang, J. Wang, F. Wang, Y. Chen, S. Zhang, C. Jiang, *Adv. Funct. Mater.* **2021**, *31*, 2005662.
- [43] X. J. She, C. Chen, G. Divitini, B. Zhao, Y. Li, J. Wang, H. Sirringhaus, *Nat. Electron.* **2020**, *3*, 694.
- [44] A. Axt, I. M. Hermes, V. W. Bergmann, N. Tausendpfund, S. A. Weber, *Beilstein J. Nanotechnol.* **2018**, *9*, 1809.
- [45] L. Bürgi, H. Sirringhaus, R. H. Friend, *Appl. Phys. Lett.* **2002**, *80*, 2913.
- [46] S. A. Weber, I. M. Hermes, S. H. Turren-Cruz, C. Gort, V. W. Bergmann, L. Gilson, R. Berger, *Energy Environ. Sci.* **2018**, *11*, 2404.
- [47] H. H. Choi, K. Cho, C. D. Frisbie, H. Sirringhaus, V. Podzorov, *Nat. Mater.* **2018**, *17*, 2.
- [48] J. L. Garrett, J. N. Munday, *Nanotechnology* **2016**, *27*, 245705.